

# Automated Tabletop Exfoliation and Identification of Monolayer Graphene Flakes

E.D.S. Courtney,<sup>1,2</sup> M. Pendharkar,<sup>1,3</sup> N.J. Bittner,<sup>4</sup> A.L. Sharpe,<sup>5</sup> and D. Goldhaber-Gordon<sup>1,2</sup>

<sup>1)</sup>*Stanford Institute for Materials and Energy Sciences, SLAC National Accelerator Laboratory, Menlo Park, CA 94025*

<sup>2)</sup>*Department of Physics, Stanford University, Stanford, CA 94305*

<sup>3)</sup>*Department of Materials Science and Engineering, Stanford University, Stanford, CA 94305*

<sup>4)</sup>*Independent Researcher*

<sup>5)</sup>*Materials Physics Department, Sandia National Laboratories, Livermore, CA 94550*

(\*Electronic mail: elijahc [at] stanford [dot] edu)

(\*Electronic mail: goldhaber-gordon [at] stanford [dot] edu)

(Dated: 20 March 2024)

The discovery of graphene, one of the most-studied materials in condensed matter physics due to its singular mechanical, optical, and electronic properties, was enabled by manual “Scotch Tape” exfoliation. Nearly two decades later, this method is still widely used to obtain chemically-pristine flakes of graphene and other 2D van der Waals materials. Unfortunately, the yield of large, pristine flakes with uniform thickness is inconsistent. Thus, significant time and effort are required to exfoliate and locate flakes suitable for fabricating multilayer van der Waals heterostructures. Here, we describe a relatively affordable tabletop device (the “eXfoliator”) that can reproducibly control key parameters and largely automate the exfoliation process. In a typical exfoliation run, the eXfoliator produces 3 or more large ( $\geq 400 \mu\text{m}^2$ ) high-quality monolayers, allowing new users to produce large pristine graphene monolayers at a rate comparable to manual exfoliation by an experienced user. We use an automated mapping system and computer vision algorithm to locate candidate flakes.

## I. INTRODUCTION

Monolayer graphene, a single layer of carbon atoms arranged in a uniform honeycomb lattice with an atomic spacing of  $1.42\text{\AA}$ , has remarkable mechanical, optical, and electronic properties. Graphene has recently emerged as an exciting basis for studying strongly-correlated electron physics. Naturally occurring stacking orders of multi-layer graphene, such as Bernal bilayer graphene, ABC-trilayer graphene, and pentalayer rhombohedral graphene, can display superconductivity<sup>1–3</sup> and orbital magnetism<sup>4,5</sup>. In addition to these configurations exfoliated from natural graphite, monolayer graphene can be artificially stacked with interlayer twists to form moiré materials with a large structural design space, including configurations with flat electronic bands and non-trivial band topology. Superconductivity and orbital magnetism<sup>6,7</sup>, and hints of fractional Chern insulators<sup>8,9</sup>, have been discovered in various graphene-based moiré materials. Motivated by the rich set of target structures based on this single material, we base our discussion and experimental demonstration on graphene, but we anticipate our methods and workflow will apply more broadly to the burgeoning family of exfoliable van der Waals layered materials.

In the Scotch tape exfoliation method introduced by Geim and Novoselov in 2004<sup>10</sup>, natural or man-made graphite crystals — which may consist of  $10^4$ – $10^6$  graphene layers arranged in large crystallographic domains — are repeatedly adhered to adhesive tape and cleaved apart to populate large areas of the tape with increasingly thin graphite crystals. The graphite-populated surface of the tape is then applied to a Si wafer coated with a thin  $\text{SiO}_2$  layer. The tape-graphite-wafer sandwich is then annealed, typically to approximately  $100^\circ\text{C}$ , before the tape is peeled away. Graphene flakes with a dis-

tribution of thicknesses ranging down to just one layer cleave from the graphite and are left on the wafer, when adhesion to the  $\text{SiO}_2$  overcomes interlayer binding in the graphite.

Other techniques for producing large-area monolayers from bulk graphite, including electrostatic exfoliation, gold-tape exfoliation, intercalation, and sonication continue to be developed, and graphene can also be grown over large areas by CVD. Each of these techniques has its own advantages, as discussed below, but Scotch tape exfoliation remains pre-eminent when seeking low disorder graphene-based structures in a research – as opposed to industrial production – environment. However, with the exception of CVD growth, these methods are inherently limited by the size of domains in the source graphite crystal.

Electrostatic exfoliation uses high potentials between two metallic electrodes to directly cleave graphite into mono- and few-layer graphene flakes, but often results in smaller flakes with higher numbers of defects, especially in monolayers<sup>11</sup>. The limited size and low quality of resulting monolayers render this technique ill-suited to produce flakes destined for twisted bilayer graphene or other multilayers with delicate electronic structure.

Both metal-assisted and gold-tape exfoliation techniques can produce large monolayers of TMD materials; furthermore, nickel-assisted exfoliation has been used to successfully extract single-crystal graphene monolayers from bilayer graphene grown on  $\text{SiC}(0001)$ <sup>12</sup>. These techniques depend on strongly adhering the target monolayer to a metal film. The monolayer is subsequently transferred to a new substrate and the metal film chemically etched, but complete removal of the metal and etchant typically cannot be accomplished without damaging the graphene. Sonication and intercalation to extract monolayer graphene leave adsorbates on the graphene

and often result in flakes smaller than 1 micron<sup>12,13</sup>, again undesirable when planning to stack it into multilayers and study exotic electronic states.

Large-area growth techniques have produced promisingly large single-crystal graphene monolayers on a variety of substrates<sup>14–16</sup>. Transfer of these monolayers to silicon has typically involved solvents and sometimes etchants. Dry transfer, most suitable for seeking exotic electronic states, has been rare for these grown films, despite notable successes in oxidizing a copper growth substrate then picking up graphene using exfoliated hBN<sup>17</sup>.

The design of a tabletop machine to perform Scotch tape exfoliation was primarily inspired by the observation that the Scotch tape exfoliation process takes considerable time and has inconsistent yields. We hypothesized that if the key parameters of the exfoliation process could be identified, optimal values could be determined through experiments using a purpose-built tool, and then reproduced in successive exfoliations with that tool. By translating exfoliation to a semi-automated process run on a machine, a single standardized exfoliation could produce more large single-crystal freestanding monolayers than a series of manual exfoliations, in a comparable amount of time. Furthermore, the search for optimal parameters need only be carried out once, so a sufficiently accessible design would allow individual operators to exfoliate near-optimally after a much shorter learning period than that required for manual exfoliation. Additionally, if optimal parameters existed outside the range that a human researcher could implement consistently in manual exfoliation (e.g., peeling at 0.1 mm/s or maintaining the chip at 80°C during peeling), a machine might be able to achieve better results than even experienced practitioners of manual exfoliation. Finally, such a machine would free the operator to pursue other work while running an otherwise tedious or time-consuming exfoliation recipe.

In fact, based on similar considerations, others have already implemented automated exfoliation systems.

A prominent example of automated exfoliation is Brookhaven's Quantum Material Press (QPress)<sup>18</sup>, a sophisticated cluster of almost fully automated tools capable of exfoliating, cataloguing, stacking, and storing 2D materials in an inert atmosphere. QPress has successfully automated most of the tape exfoliation process, is accessible through user proposals, and may eventually provide flakes to many collaborators. In the opposite limit, a simple automated exfoliation tool can consist of a single linear motor in tandem with a hot plate<sup>19</sup>.

The tool presented in this paper (the "eXfoliator") was designed to fill a middle ground, as a user-friendly machine capable of controlling a range of likely-relevant parameters during exfoliation, balancing practicality and utility as an exfoliation tool with simplicity of design and construction. The parameters of Scotch tape exfoliation targeted by the design are peel angle, peel rate, application pressure, temperature of the substrate at all stages, and dwell time under pressure or at temperature.

Estimates of graphite's interlayer van der Waals binding energy vary, but most calculated values for AB, AAA, and ABC-stacked graphite range from 40-60 meV/atom<sup>20</sup>. For

comparison, the thermal energy of graphite at 300 (400) K is approximately 1300 (2400) J/mol, corresponding to 13.5 (25) meV/atom<sup>21</sup>. Because the thermal energy at accessible temperatures – as limited by the melting point of the tape's backing – does not cross or approach the binding energy threshold, tuning the annealing or peeling temperature is assumed to primarily affect the viscoelastic behavior of the polymer tape adhesive.

From the time-temperature superposition principle of polymer flow<sup>22</sup>, adjusting the annealing temperature, application pressure, or dwell time is believed to allow the viscoelastic polymer tape adhesive to flow more freely over the graphite flakes and allow better contact before being cooled and peeled. Likewise, adjusting peel speed is assumed to tune the viscoelastic behavior of the tape adhesive instead of significantly affecting the fundamental interlayer interactions of the graphene layers. Adjusting the peel angle is believed to both change the radius of curvature of the tape and change the ratio of shearing to normal forces at the interlayer boundary.

Graphene is typically manually exfoliated onto cleaved chips of crystalline material (such as silicon), each with an area of a few cm<sup>2</sup>. The eXfoliator exfoliates over a 50x50 mm square (25 cm<sup>2</sup> area, 5-20x that in a typical manual exfoliation) on a 76 mm diameter Si/SiO<sub>2</sub> wafer. The increased scale was chosen in tandem with the purchase of a microscope with a motorized stage, capable of imaging contiguous areas as large as 8 cm on a side. To leverage this capability, a computer-vision algorithm was developed to reliably identify images containing monolayer graphene flakes by empirically relating local substrate color to monolayer appearance and identifying contiguous clusters of pixels, allowing for more efficient evaluation of exfoliations and reducing both labor and time required to locate the largest monolayers on the substrate. The imaging and flake identification will be described elsewhere, but similar techniques have been previously demonstrated<sup>23</sup>.

In an ideal exfoliation of a van der Waals material, single-crystal flakes of the desired thickness – often, as here, monolayer – are cleaved from thicker crystals on the populated tape by adhesion to the substrate. The resulting size, integrity, cleanliness, and number density of these flakes on the substrate thus characterize the success of the exfoliation attempt.

## II. MATERIALS AND METHODS

The Scotch tape exfoliation process described here entails creating graphite-covered tape, applying the populated tape to an oxidized silicon substrate, annealing the tape-silicon system, and subsequently peeling the tape from the silicon. The silicon substrate must then be searched to locate resulting monolayers, which can be picked up and used to create graphene-based devices.

### A. The eXfoliator

The eXfoliator uses three perpendicular linear stepper motors (Fig. 1B, Parts 3,9) mounted on a metal frame (Parts 1-2,4-8) to move an extended arm (Parts 10-16) above a remotely controlled hot plate (Part 17) with a custom machined aluminum working surface (Parts 18-21). The machine itself occupies a nearly cubic volume of 46x54x51 cm. The motors, force gauge, and hot plate are connected to an external computer running a custom GUI to facilitate operation, including both manual and scripted control with recipes that can be standardized.

The hot plate used in this work was initially selected for its advertised heating and weighing functions with digital control; however, the weighing function was determined to be unreliable, necessitating incorporating a separate force gauge. Additionally, the time to reach temperature set points was substantially increased relative to the hot plate's initial performance due to the additional thermal mass and surface area of the plate adapter and wafer pedestal (Parts 18-19). For future implementations of the eXfoliator design, we suggest considering other hot plates with increased heating power to more quickly reach temperature set points; a minor redesign of Part 18 will be required to accommodate a different working surface.

As shown in Figure 1B, the presented design was modified to improve cooling, thereby more closely approximating a common method of manual exfoliation where the tape-silicon sandwich is removed from the hot plate and allowed to cool within seconds prior to peeling. However, even the modified version took nearly 25 minutes to cool from 105°C to below 30°C; incorporating active cooling may prove beneficial.

### B. Graphene Exfoliation

In Scotch tape exfoliation, natural graphite crystals are repeatedly adhered to adhesive tape and cleaved apart to populate a large area of the tape with successively thinner graphite crystals; as this process roughly doubles the graphite-populated area of tape with each cleave, a 25 cm<sup>2</sup> area may be fully populated in as few as 8 cleaves from a 9 mm<sup>2</sup> starting crystal. The eXfoliator was designed to be able to populate two 25 cm<sup>2</sup> areas of tape simultaneously, but the process proved too inefficient compared to manually populating the tape. Therefore, for all results reported here, we manually populated an initial 'mother tape', which we then used to populate a 25 cm<sup>2</sup> 'daughter tape' to be used in the eXfoliator, a process analogous to that commonly used in manual exfoliation. The materials used by the eXfoliator in this paper are also commonly used in manual exfoliation: 1" Scotch magic tape, "flaggy" graphite flakes purchased from NGS Trading & Consulting, and 76mm silicon wafers topped with 300nm wet silicon oxide purchased from NovaWafers. However, the eXfoliator's design does not limit it to these materials. We envision that the eXfoliator can be easily used to exfoliate most vdW materials, including hBN and transition metal dichalcogenides, onto a wide variety of substrates using a wide variety

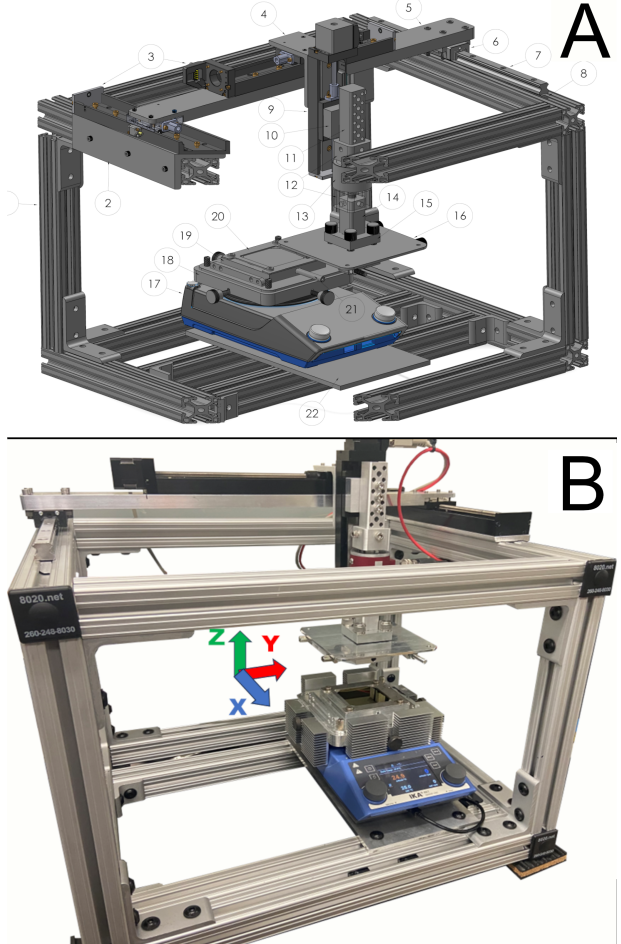


FIG. 1. A. A schematic of the eXfoliator with key parts labeled; see Appendix A for the parts list. CAD files are provided through the Stanford Digital Repository<sup>24</sup>. B. The constructed eXfoliator, with populated tape prepared to be pressed to a silicon wafer. The peeling motion takes place in the Y-Z plane. Aluminum fin comb heatsinks were added to the hot plate to speed cooling with the aid of a small external fan (not shown).

of adhesive surfaces to hold the initial material.

During operation, a pristine 76 mm Si/SiO<sub>2</sub> wafer is clamped in place on the wafer holder (Part 19) by Part 20. The daughter tape is mounted to the tape plate (Part 16) and populated in place; the tape plate is then mounted to the moving arm using Part 15, with four intervening wave springs to increase uniformity of contact as pressure is applied. The tape plate is positioned over the target substrate using the GUI, and the tape can then be applied to the substrate at a desired pressure,  $P$ , annealed at a desired temperature,  $T$ , and peeled at a desired rate,  $V$ , at an angle  $\theta$  in the Y-Z plane, defined as the angle formed by the tape with respect to the Y-axis as the tape is peeled from the substrate. Typical usage used a range of peel speeds and anneal temperatures, but targeted a 30 kPa application pressure, annealing over the time required to cool from the set temperature to within 5°C of the desired peeling temperature of 25°C, and a peel angle that was varied continuously from 60° to 80° over each exfoliation.

Parameter	Min	Max	Typical	Manual
$P$	400 Pa	40 kPa	30 kPa	1-10 kPa
$T$	25°C	200°C	25-100°C	90°C
$V$	1 $\mu\text{m}/\text{s}$	1.2 $\text{cm}/\text{s}$	1 $\mu\text{m}/\text{s}$ -1 $\text{cm}/\text{s}$	1 mm/s
$\theta$	60°	170°	60-80°	30-170°

TABLE I. Exfoliation parameters considered in this study, with the extreme values accessible by eXfoliator, typical values used in this study, and representative values for manual exfoliation.

After the tape is peeled, the wafer with exfoliated graphene is transferred to the motion stage of a Leica DM6 M microscope. The area on the wafer where exfoliation is performed is then scanned at 10x magnification with a flat-field correction to equalize brightness, and constant values for exposure, gain, white balance, gamma, color saturation, and illumination intensity. A focus map for the scan area is made using between 10 and 50 manually determined XYZ values as focal points across the wafer's surface. Each scan generates approximately 3200 24-bit 20MP images per wafer to be analyzed by a flake-finding algorithm we designed for this purpose<sup>25</sup>.

### C. Wafer Imaging and Monolayer Identification

It is well known that the optical transmission of monolayer graphene is an approximately constant 97.7% for wavelengths in the visible range<sup>26</sup>. However, beginning with Geim and Novoselov's work<sup>10</sup>, most researchers exfoliate on silicon wafers with thin oxide to improve contrast, as the reflection from the underlying silicon roughly doubles apparent contrast, and thin-film interference effects from the oxide layer - which is typically about 90 or 300nm thick - further enhance visibility, enabling monolayer graphene to be seen through standard optical microscopes without heavy image processing.

For the purpose of automating flake detection, it is beneficial to choose lighting conditions and camera settings to further enhance contrast. All imaging used the provided LED illumination of the Leica DM6 M and a 10x magnification objective (Leica Objective #566503, NA 0.3). In software, a flat-field correction was applied to all images in order to remove vignetting, and a suitable white-balance of the images was chosen and held constant through the study, resulting in all images being saved in false-color and enhancing monolayer contrast against the silicon background.

Though all sample wafers have nominally uniform 300nm thick layers of silicon oxide, it was noted during the study that the manufacturer's specified tolerance of  $\pm 5\%$  oxide thickness resulted in varying background colors within individual wafers and from wafer to wafer. Thus, it was necessary to determine empirical relations between apparent background and monolayer color across a range of backgrounds. These relations were initially determined by collecting over 200 monolayer-background color pairs from the output of a less accurate algorithm across several samples, and were then held fixed throughout the experiment.

The computer vision (CV) algorithm detects the background color in each image, and uses the previously calculated

empirical linear relations between background and monolayer colors in the R, G, and B channels under the established lighting settings to predict monolayer appearance. Clusters of pixels within a certain Euclidean distance of the predicted flake color were then identified and labeled, with the corresponding image saved for subsequent review.

All images identified as containing monolayers were manually categorized to identify freestanding monolayers and eliminate false positives before being uploaded to a shared repository for use in device fabrication; a wafer-scale stitched image was generated for each sample with labeled flake locations to facilitate retrieval, as shown in Figure 2.

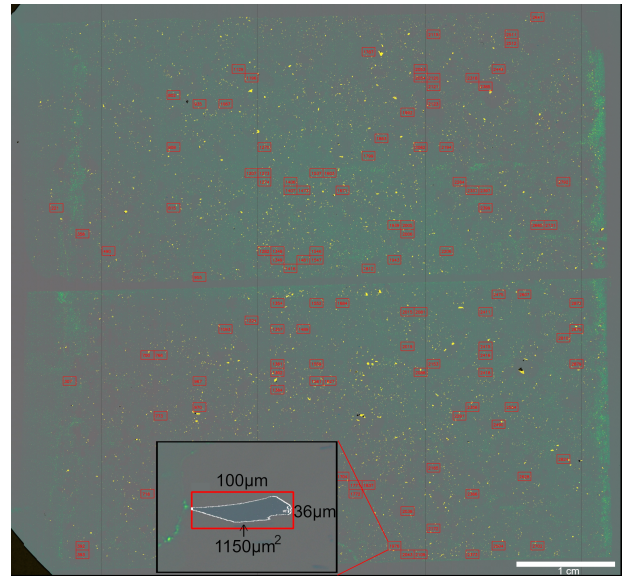


FIG. 2. A composite, false-color image of the scanned area on an exfoliated wafer, with identified monolayer locations highlighted in red and labeled according to the image's location in the wafer scan. Scale bar corresponds to 1 cm. This wafer was annealed at 25°C and peeled at 100  $\mu\text{m}/\text{s}$  with a contact pressure of 29 kPa and a peel angle swept from 60°-80°. Inset: a monolayer graphene flake with a calculated area of  $1150\mu\text{m}^2$  and bounding box.

As discussed in Results, the algorithm was less reliable in detecting monolayers with areas below  $100\mu\text{m}^2$  - corresponding to a smallest length dimension of 5-10 pixels. However, the most desirable monolayers for assembling TBG stacks are typically above  $400\mu\text{m}^2$  in area. We accordingly chose  $200\mu\text{m}^2$  as the cutoff value above which we presumed all flakes were found. In addition to this dependence on area, other significant limitations of the algorithm include sensitivity to lighting settings and a failure to detect monolayers located on backgrounds outside the range used to determine the initial empirical relations. Prepared samples were excluded from the study if large discolored areas with no detected monolayer flakes were present while other regions of the sample exhibited a significant distribution of monolayer flakes, as this indicates a failure of the flake-finding algorithm due to background color. However, as the background color is not affected by any step of the exfoliation process (including anneals up to 105°C), this is not expected to bias the reported

results. For further details on the flake-finding algorithm, see Bittner et al. (2024), in preparation<sup>25</sup>.

### III. RESULTS

In total, 33 sample wafers were created over a range of peel speeds and anneal temperatures, as shown in Table II. All wafers were created by applying the populated tape with an average pressure  $P = 29 \pm 2$  kPa and peeling with an angle  $\theta$  that repeatably swept from  $60^\circ$  to  $80^\circ$  across each wafer.

Based on the empirical observation that various manual exfoliation techniques seem to produce similar results, the parameter space for exfoliation appears to be fairly flat. That is, while different techniques and user experience may moderately increase flake yield per  $\text{cm}^2$ , it is expected that no dramatically optimal parameters will be found. Thus, it was deemed satisfactory to find a point in parameter space that produces a number of large, freestanding monolayers with low levels of polymer residue at a rate comparable to both manual exfoliation, and sufficient to feed the pipeline of device fabrication in the lab.

Count (N)	1 $\mu\text{m}/\text{s}$	10 $\mu\text{m}/\text{s}$	100 $\mu\text{m}/\text{s}$	1 cm/s	Total
25°C	2	7	8	4	21
65°C	4	1	2	1	8
105°C	1	1	1	1	4
Total	7	9	11	6	33

TABLE II. Number of sample wafers exfoliated at each peel speed and anneal temperature, with application pressure, dwell time, peel angle, and peel temperature held constant.

After exfoliation, the CV flake searching algorithm was applied and the freestanding monolayers of area greater than  $200 \mu\text{m}^2$  ("useful" monolayers) tabulated, with average yields per wafer shown in Table VII (see Appendix B).

As the graphite crystals used in this experiment were all formed by natural processes, it is expected that the size of crystal domains therein will vary, an expectation born out by cursory examinations of the distribution of flake areas, as exfoliated monolayer graphene flakes are typically single-crystal. Furthermore, repeatedly cleaving a flake via adhesion to tape during the population step naturally leads to a distribution of flake dimensions. This can be seen by considering a simple model of an  $N$ -layer crystal as cleaving into fractions of thickness  $\alpha N$  and  $(1 - \alpha)N$  for some positive constant  $\alpha < 1$ . Using this model, upon repeated cleaving steps - as occur during tape population - the probability  $\mathcal{P}_k$  to find a flake of thickness  $t_k = N\alpha^k(1 - \alpha)^{n-k}$  after  $n$  cleaves is given by  $\mathcal{P}_k = \frac{1}{2^n} \frac{n!}{k!(n-k)!}$ , where values of  $t_k < 1$  represent monolayers with areas smaller than the starting crystal. This inevitable distribution of flake thickness (and monolayer areas) is further compounded by differences in flake thickness and crystal domain size in the starting graphite, and may account for some of the variance seen in the observed yields.

To account for this inherent variance in the manual population step, the useful monolayer counts were then normalized

by the area of graphite remaining on the populated tape post-exfoliation as a proxy for the initial graphite area. As shown in Table III, slower peel speeds tend to yield more useful monolayers.

UML/A <sub>graphite</sub> (N/mm <sup>2</sup> )	1 $\mu\text{m}/\text{s}$	10 $\mu\text{m}/\text{s}$	100 $\mu\text{m}/\text{s}$	1 cm/s	Mean
25°C	1.7 ± 0.1	2.4 ± 1.6	1.4 ± 0.9	0.7 ± 1.2	1.6 ± 1.3
65°C	3.4 ± 0.8	2.9	2.6 ± 1	1.8	2.8 ± 0.9
105°C	2.9	0.9	1.6	2.2	1.6 ± 0.9
Mean	2.8 ± 1	2.2 ± 1.5	1.5 ± 1	1.1 ± 1	1.8 ± 1.3

TABLE III. Number of useful monolayers per square mm of graphite on the initial tape at each parameter.

As shown in Tables IV and V, no clear relationship between peel speed or anneal temperature and individual monolayer area is evident in this experiment. As shown in the preceding

$\langle A_{UML} \rangle (\mu\text{m}^2/\text{flake})$	1 $\mu\text{m}/\text{s}$	10 $\mu\text{m}/\text{s}$	100 $\mu\text{m}/\text{s}$	1 cm/s	Mean
25°C	430 ± 180	370 ± 50	490 ± 210	470 ± 210	430 ± 160
65°C	470 ± 180	410	370 ± 50	440	440 ± 130
105°C	460	380	440	360	420 ± 50
Mean	460 ± 150	380 ± 50	460 ± 180	440 ± 170	430 ± 140

TABLE IV. Average area of a useful monolayer at each parameter.

tables, the standard deviations of most measured metrics are comparable to the mean observed values; while this precludes strong conclusions about the dependence of yield on peel speed or anneal temperature, some weak trends may still be observed. This is clarified by calculating Pearson's product-moment correlation coefficient  $r$ , which describes the strength of linear associations between two variables - true positive (negative) linear dependence is represented by  $r = 1(-1)$ , with a total lack of dependence represented by  $r = 0$ . Here, while absolute values of  $|r| \approx 0.25$  indicate a weak relationship between peel speed and normalized UML yields, it is clear that an uncontrolled variable is strongly affecting actual results. We presume this to be the inherent variance of tapes manually populated with natural graphite, though other uncontrolled factors such as ambient humidity or substrate contamination may also contribute. Though monolayer yield per

$r$	$\langle N_{UML} \rangle$ (N/wafer)	UML/A <sub>gr</sub> (N/mm <sup>2</sup> )	A <sub>UML</sub> /A <sub>gr</sub> ( $\mu\text{m}^2/\text{mm}^2$ )	UML Yield (%)	$\langle A_{UML} \rangle$ ( $\mu\text{m}^2/\text{flake}$ )
T	0.18	0.13	0.07	-0.08	-0.02
V	-0.34	-0.32	-0.28	-0.24	0.001

TABLE V. Pearson product-moment correlation coefficients  $r$  between controlled variables  $T, V$  and the respective dependent variables.

wafer seems to somewhat increase at slower peel speeds and 65°C, the increase in residue and added (unattended) time per exfoliation favors using higher peel speeds and lower temperature anneals. Aside from the annealing and peeling steps, typical sample preparation for the eXfoliator took approximately 15 minutes, with another 60 minutes post-exfoliation

to scan and search each wafer. As the eXfoliator can be prepared and run in parallel with the mapping microscope, maximum sample production is in practice reached by all recipes that take less than 45 minutes to complete. With the approximate time to complete each recipe given by Table XII, this limits efficient exfoliation recipes to peel speeds of  $100 \mu\text{m/s}$  or higher. As there is no strong correlation between individual monolayer area and anneal temperature or peel speed, the figure of merit for this study is taken to be number of monolayers per starting area of graphite; as shown in Table III, annealing at  $65^\circ\text{C}$  seems to yield better results than the other temperatures. However, because tape adhesive is a viscous polymer that readily flows at these temperatures, slower peel speeds and higher anneal temperatures result in increased levels of polymer residue on the wafer, as shown in Figure 4. Monolayers are primarily cleaved from the bottom of larger flakes and are thus often pristine regardless of the amount of residue elsewhere on the wafer, but stamp-based stacking techniques are often hindered by the presence of thick tape residue nearby. We have no solvent-free technique for reliably removing heavy polymer residue left by Scotch magic tape without damaging flakes, so it is desirable to use exfoliation recipes that minimize tape residue while retaining sufficient yield of flakes. With the additional constraints of time and residue, the preferred exfoliation recipe explored in this study was determined to be annealing at  $25^\circ\text{C}$  and peeling at  $100 \mu\text{m/s}$ .

Overall, approximately 35% of all monolayers detected with areas greater than  $200 \mu\text{m}^2$  were freestanding, useful monolayers. As shown in Appendix C, the total and useful monolayer yield per wafer of most parameter pairs did not significantly deviate from the average, suggesting that peel speed and anneal temperature are not the dominant causes of flake area distribution. The effect of uncontrolled variables, such as humidity and initial graphite thickness, was not examined in this study, but the eXfoliator design allows for further investigation if desired.

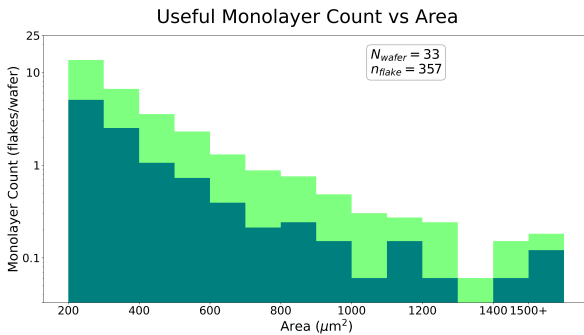


FIG. 3. A histogram of flake area, normalized to wafer count with  $100 \mu\text{m}^2$  bins. The distribution of useful monolayers (blue) is shown against that of all monolayers detected (green), with a final proportion of 357/1014. Parameter-wise histograms are given in Appendix C.

#### IV. CONCLUSIONS

This paper introduced a simple, compact device for the semi-automated exfoliation of monolayer materials, further describing the imaging system used to characterize the performance of the device across a range of parameters. Overall, the eXfoliator system successfully produces sufficient numbers of large, freestanding monolayers for use in device fabrication, with an output of approximately three large monolayers per wafer. The eXfoliator is believed to improve reproducibility and throughput compared to manual exfoliation, but further studies of flake yield with significantly more samples or a more reproducible technique for populating the initial tape are required. The eXfoliator retains accessibility, with new users typically requiring three or fewer sample preparations to reach near-maximum efficiency. As manual exfoliation may take months or years for a user to reach a similar rate of flake production, the eXfoliator should have significant utility in labs whose research intensively relies on high-quality graphene monolayers. Unlike Brookhaven's QPress, the eXfoliator is not presently operated in an inert gas atmosphere, but its small footprint allows for placement into a glove-box if exfoliation of air-sensitive materials is desired.

The investigation of flake production as a function of anneal temperature and peel speed revealed that Scotch tape exfoliation does not strongly depend on these two factors at the parameter values investigated. In practice, the production rate of useful monolayers was most heavily affected by the total time to exfoliate each sample wafer and the amount of polymer tape residue remaining on an exfoliated wafer.

The eXfoliator's design is well-suited for production of other van der Waals' materials, such as hexagonal boron nitride and transition metal dichalcogenides, and allows for further exfoliation studies using other substrates, materials, and parameters. Current limitations of the eXfoliator design include its low cooling rate, placing a lower limit on the tape-silicon dwell time for elevated temperatures, and lack of an implemented rotational degree of freedom in the Y-Z plane, which prevents 'roll-on' techniques to apply populated tape to silicon from being implemented.

#### V. ACKNOWLEDGMENTS

The authors thank Chaitrali Duse and Steven Tran for their aid in preparing several samples; Joe Finney, Rupini Kamat, and Greg Zaborski Jr. for their insight and feedback in designing a machine to replicate manual exfoliation of monolayer graphene; Andy Mannix for useful discussions about the exfoliation process; and Feng Wang, Jingxu Xie, and Emma Regan for useful discussions about the reasoning behind their exfoliator's design. Experimental measurements and analysis, parts for building the automated exfoliator, and acquisition of the motorized microscope for efficient imaging of the output of the exfoliator, were supported by the U.S. Department of Energy, Office of Basic Energy Sciences (DE-SC0021984). Supporting infrastructure was funded in part by the Gordon and Betty Moore Foundation through Grant No. GBMF3429.

## VI. APPENDIX A - EXFOLIATOR PARTS

1. Aluminum 1515 t-slot frame - 4× 12" rails, 10× 18" rails, with appropriate right-angle brackets
2. Aluminum VT-50L mount, custom machined
3. Translation Stage VT-50L, 200mm travel, via MicronixUsa
4. Aluminum XZ bracket, custom machined
5. Aluminum crossbeam, custom machined
6. Flanged ball bearing carriage, via McMaster-Carr (6709K11)
7. 340mm carriage guide rail, via McMaster-Carr (6709K33)
8. Guide rail mount for t-slot frame, via McMaster-Carr (1748N14)
9. Translation Stage VT-50L, 100mm travel, via MicronixUsa
10. Aluminum standoff, custom machined
11. Aluminum upper post, custom machined
12. Aluminum load cell mount, custom machined
13. LCF300 25lb universal load cell, via FUTEK (FSH04274) with USB cable and output (FSH04720, FSH04742)
14. Aluminum lower post, custom machined
15. Aluminum post mount, custom machined
16. Aluminum tape plate, custom machined
17. RET Control Visc hot plate, via IKA (0005020001)
18. Aluminum plate adapter, custom machined
19. Aluminum wafer pedestal, custom machined
20. Aluminum wafer pedestal top, custom machined

Note: We encountered a software bug in the firmware of the hotplate which made it insensitive to minor incremental changes in weight. Given that our design relied on making gradual contact with live feedback from the weight sensor, the hot plate could not be used for its originally intended purpose of providing both computerized temperature control and force feedback, inspiring the incorporation of a load cell.

21. Aluminum temperature probe sabot, custom machined
22. Aluminum mounting plate, via McMaster-Carr

## VII. APPENDIX B - ADDITIONAL TABLES

Count (N)	1 $\mu\text{m/s}$	10 $\mu\text{m/s}$	100 $\mu\text{m/s}$	1 cm/s	Total
25°C	2	7	8	4	21
65°C	4	1	2	1	8
105°C	1	1	1	1	4
Total	7	9	11	6	33

TABLE VI. Number of sample wafers exfoliated at each peel speed and anneal temperature, with application pressure, dwell time, peel angle, and peel temperature held constant.

$\langle N_{UML} \rangle$ (N/wafer)	1 $\mu\text{m/s}$	10 $\mu\text{m/s}$	100 $\mu\text{m/s}$	1 cm/s	Mean
25°C	10±2	13±3	9±5	5±3	10±5
65°C	14±4	17	9.5±0.7	16	14±4
105°C	10	8	16	8	11±4
Mean	12±4	13±4	10±5	8±5	11±5

TABLE VII. Number of useful monolayers per sample at each peel speed and anneal temperature, presented with standard deviations.

UML/A <sub>gr</sub> (N/mm <sup>2</sup> )	1 $\mu\text{m/s}$	10 $\mu\text{m/s}$	100 $\mu\text{m/s}$	1 cm/s	Mean
25°C	1.7±0.1	2.4±1.6	1.4±0.9	0.7±1.2	1.6±1.3
65°C	3.4±0.8	2.9	2.6±1	1.8	2.8±0.9
105°C	2.9	0.9	1.6	2.2	1.6±0.9
Mean	2.8±1	2.2±1.5	1.5±1	1.1±1	1.8±1.3

TABLE VIII. Number of useful monolayers per square mm of graphite on the initial tape at each peel speed and anneal temperature, presented with standard deviations.

The normalized counts reported in Table VIII were multiplied by the average area of useful monolayers produced at the relevant parameters. As shown in Table IX, slower peel speeds tend to yield a larger total area of monolayer graphene, but large standard deviations prevent any strong conclusions from being drawn.

$A_{UML}/A_{gr}$ ( $\mu\text{m}^2/\text{mm}^2$ )	1 $\mu\text{m/s}$	10 $\mu\text{m/s}$	100 $\mu\text{m/s}$	1 cm/s	Mean
25°C	740±240	900±730	680±870	340±520	680±730
65°C	1620±810	1190	970±220	800	1250±670
105°C	1330	350	690	800	680±410
Mean	1280±740	840±690	710±740	480±440	790±700

TABLE IX. Total area of useful monolayers per square mm of graphite on the initial tape at each peel speed and anneal temperature, presented with standard deviations.

Table X shows the percentage of all detected monolayers (including monolayers smaller than 200  $\mu\text{m}^2$  and those attached to bulk) that were useful monolayers, with slower peel speeds and an anneal temperature of 65°C tending to yield a higher proportion of useful monolayers.

UML Yield (%)	1 $\mu\text{m/s}$	10 $\mu\text{m/s}$	100 $\mu\text{m/s}$	1 cm/s	Mean
25°C	15±7	10±4	9±3	10±7	10±5
65°C	19±5	19.8	13±0.4	9.5	15±5
105°C	19.2	8.6	6.3	14	9±6
Mean	18±5	10±5	9±3	10±6	11±5

TABLE X. Yield of useful monolayers, as a percentage of all detected monolayers, at each peel speed and anneal temperature, presented with standard deviations.

$\langle A_{UML} \rangle$ ( $\mu\text{m}^2/\text{flake}$ )	1 $\mu\text{m/s}$	10 $\mu\text{m/s}$	100 $\mu\text{m/s}$	1 cm/s	Mean
25°C	430±180	370±50	490±210	470±210	430±160
65°C	470±180	410	370±50	440	440±130
105°C	460	380	440	360	420±50
Mean	460±150	380±50	460±180	440±170	430±140

TABLE XI. Average area of a useful monolayer at each peel speed and anneal temperature.

Time (min/wafer)	1 $\mu\text{m/s}$	10 $\mu\text{m/s}$	100 $\mu\text{m/s}$	1 cm/s
25°C	800	80	8	0.1
65°C	815	95	23	15
105°C	825	105	33	25

TABLE XII. Approximate time to anneal and peel a sample at each peel speed and anneal temperature, in minutes.

### VIII. APPENDIX C - ADDITIONAL FIGURES

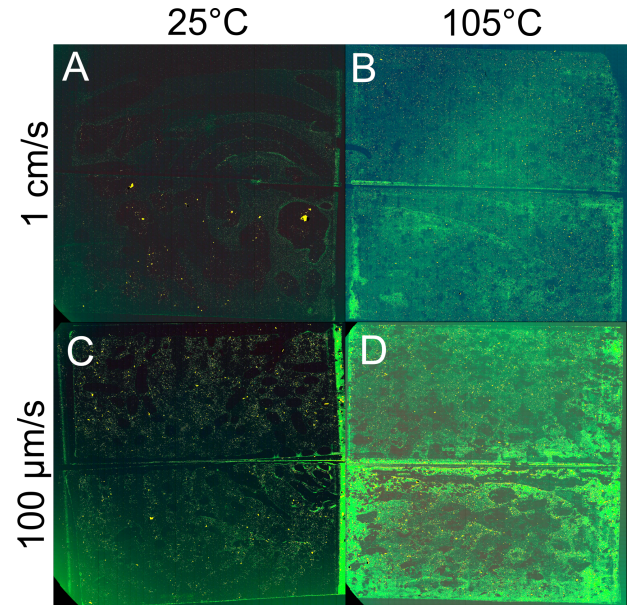


FIG. 4. Wafer-scale images of samples post-exfoliation, in false color to highlight tape residue (green), with anneal temperature and peel speed of A. 25°C and 1 cm/s, B. 105°C and 1 cm/s, C. 25°C and 100  $\mu\text{m/s}$ , and D. 105°C and 100  $\mu\text{m/s}$ . Each wafer was imaged with under identical lighting settings, with the more intense color representing thicker residue.

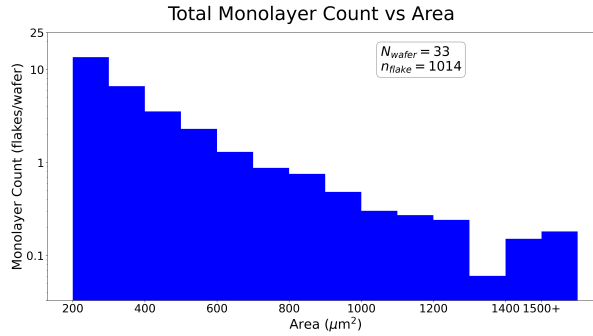


FIG. 5. A histogram of flake area with  $100 \mu\text{m}^2$  bins for all monolayers detected ( $n=1014$ ), including those attached to bulk.

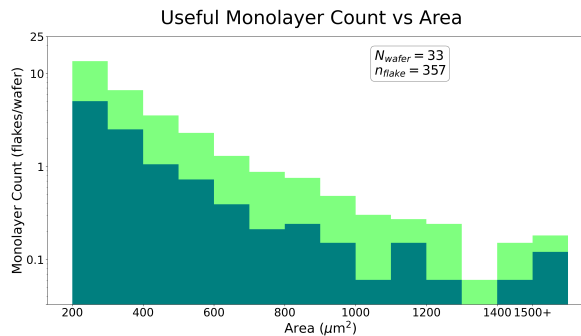


FIG. 6. A histogram of flake area with  $100 \mu\text{m}^2$  bins, identical to that shown in Fig.3. The distribution of useful monolayers (blue) is shown against that of all monolayers detected (green), with a final proportion of 357/1014.

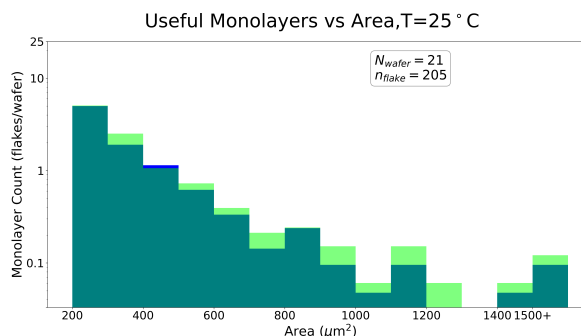


FIG. 7. A histogram of flake area with  $100 \mu\text{m}^2$  bins. The distribution of useful monolayers on wafers annealed at  $25^\circ\text{C}$  (blue) is shown against the distribution of all useful monolayers found (green).

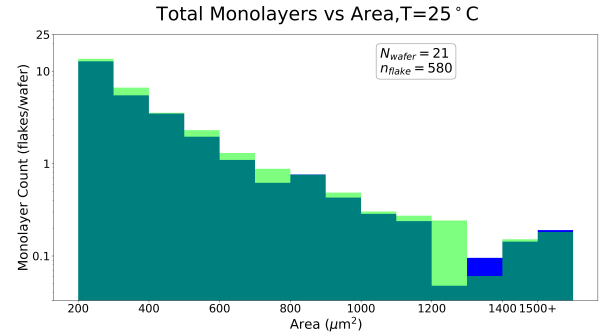


FIG. 8. A histogram of flake area with  $100 \mu\text{m}^2$  bins. The distribution of all monolayers on wafers annealed at  $25^\circ\text{C}$  (blue) is shown against the distribution of all monolayers found (green).

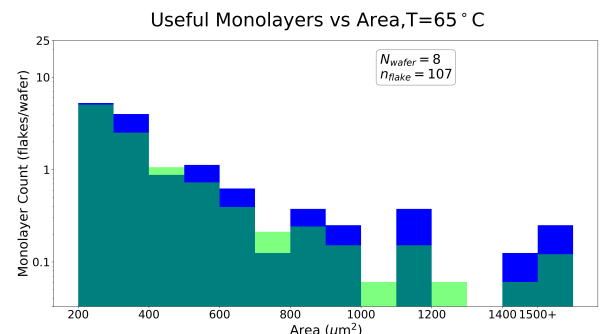


FIG. 9. A histogram of flake area with  $100 \mu\text{m}^2$  bins. The distribution of useful monolayers on wafers annealed at  $65^\circ\text{C}$  (blue) is shown against the distribution of all useful monolayers found (green).

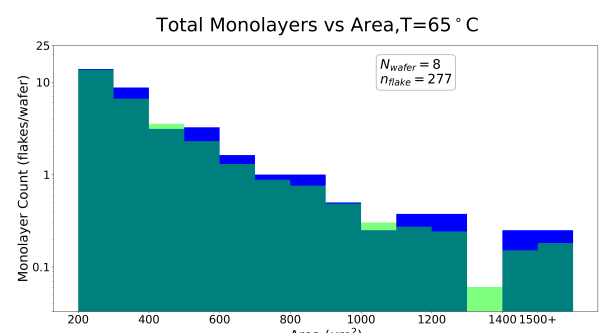


FIG. 10. A histogram of flake area with  $100 \mu\text{m}^2$  bins. The distribution of all monolayers on wafers annealed at  $65^\circ\text{C}$  (blue) is shown against the distribution of all monolayers found (green).

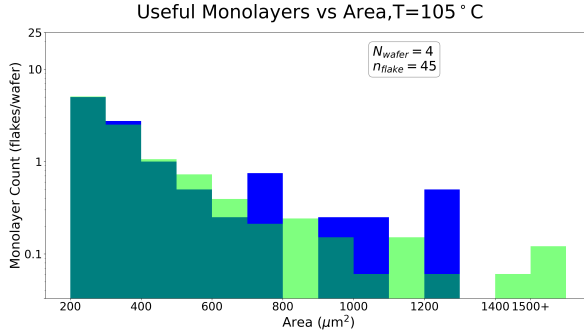


FIG. 11. A histogram of flake area with  $100 \mu\text{m}^2$  bins. The distribution of useful monolayers on wafers annealed at  $105^\circ\text{C}$  (blue) is shown against the distribution of all useful monolayers found (green).

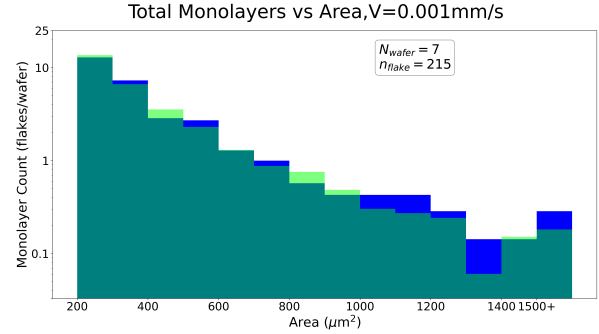


FIG. 14. A histogram of flake area with  $100 \mu\text{m}^2$  bins. The distribution of all monolayers on wafers peeled at  $1 \mu\text{m}/\text{s}$  (blue) is shown against the distribution of all monolayers found (green).

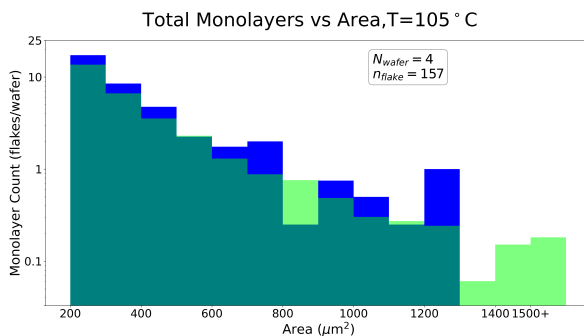


FIG. 12. A histogram of flake area with  $100 \mu\text{m}^2$  bins. The distribution of all monolayers on wafers annealed at  $105^\circ\text{C}$  (blue) is shown against the distribution of all monolayers found (green).

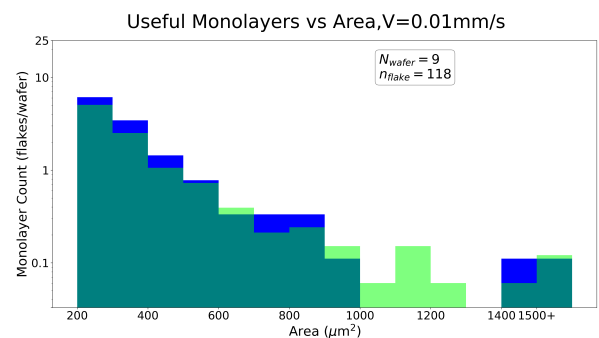


FIG. 15. A histogram of flake area with  $100 \mu\text{m}^2$  bins. The distribution of useful monolayers on wafers peeled at  $10 \mu\text{m}/\text{s}$  (blue) is shown against the distribution of all useful monolayers found (green).

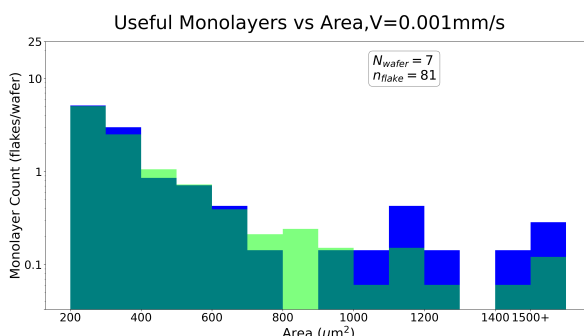


FIG. 13. A histogram of flake area with  $100 \mu\text{m}^2$  bins. The distribution of useful monolayers on wafers peeled at  $1 \mu\text{m}/\text{s}$  (blue) is shown against the distribution of all useful monolayers found (green).

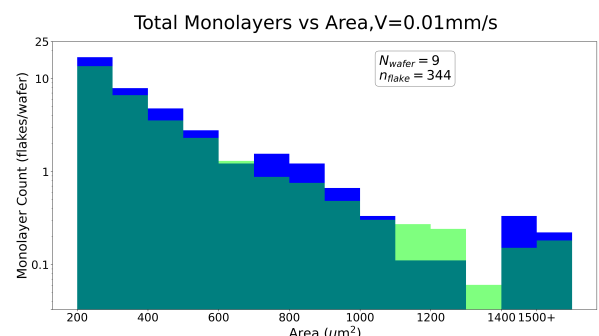


FIG. 16. A histogram of flake area with  $100 \mu\text{m}^2$  bins. The distribution of all monolayers on wafers peeled at  $10 \mu\text{m}/\text{s}$  (blue) is shown against the distribution of all monolayers found (green).

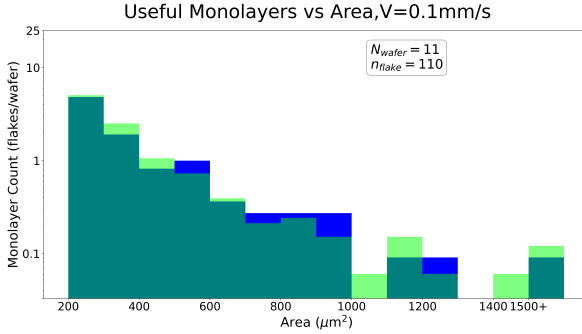


FIG. 17. A histogram of flake area with  $100 \mu\text{m}^2$  bins. The distribution of useful monolayers on wafers peeled at  $100 \mu\text{m}/\text{s}$  (blue) is shown against the distribution of all useful monolayers found (green).

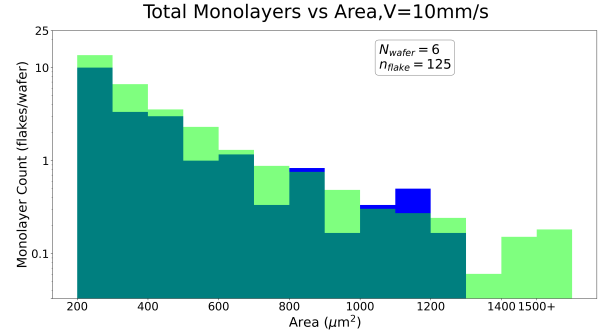


FIG. 20. A histogram of flake area with  $100 \mu\text{m}^2$  bins. The distribution of all monolayers on wafers peeled at  $1 \text{ cm}/\text{s}$  (blue) is shown against the distribution of all monolayers found (green).

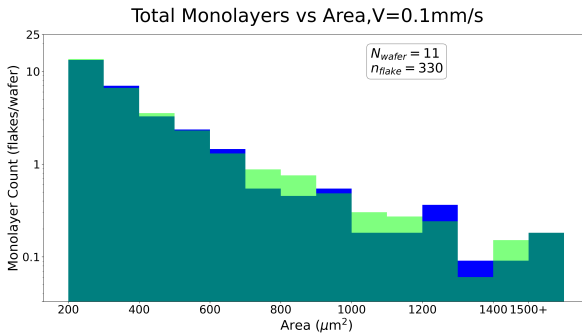


FIG. 18. A histogram of flake area with  $100 \mu\text{m}^2$  bins. The distribution of all monolayers on wafers peeled at  $100 \mu\text{m}/\text{s}$  (blue) is shown against the distribution of all monolayers found (green).

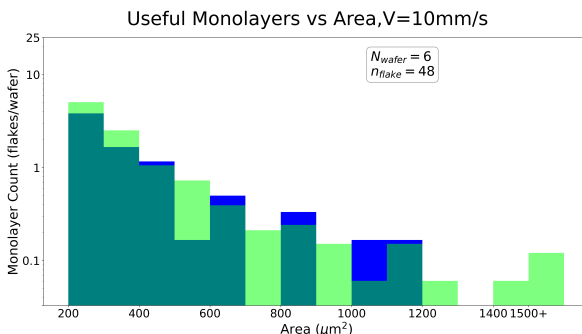


FIG. 19. A histogram of flake area with  $100 \mu\text{m}^2$  bins. The distribution of useful monolayers on wafers peeled at  $1 \text{ cm}/\text{s}$  (blue) is shown against the distribution of all useful monolayers found (green).

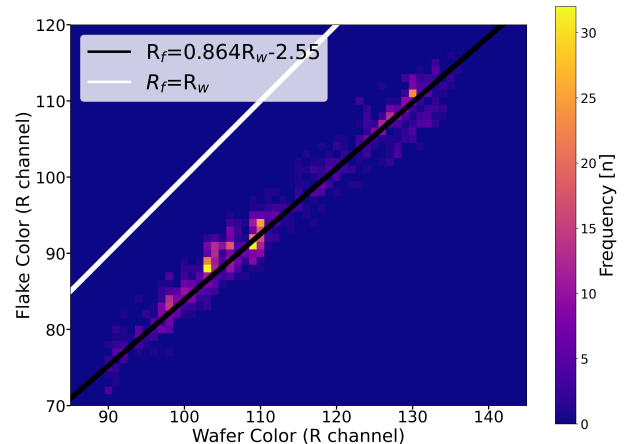


FIG. 21. Frequency of detected flake color vs local background color in the red channel. The empirical function  $R_f = 0.864R_w - 2.55$  was used to predict flake color from the background wafer color, with all pixels within Euclidean distance 8 of the predicted flake RGB passed to the cluster-finding portion of the algorithm. The apparent bimodality is due to batch differences between the two wafer cassettes used in this experiment.

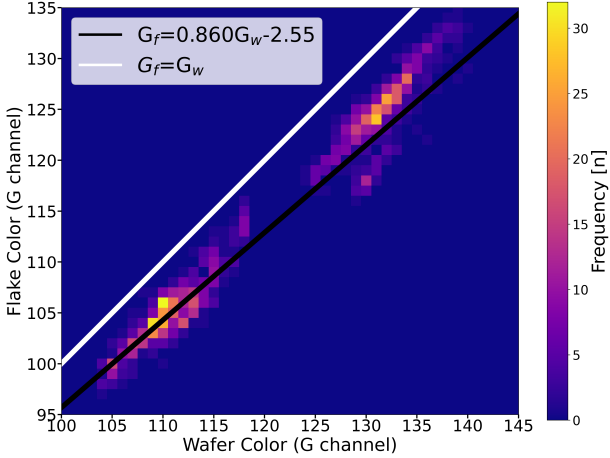


FIG. 22. Frequency of detected flake color vs local background color in the green channel. The empirical function  $G_f=0.860G_w+9.68$  was used to predict flake color from the background wafer color, with all pixels within Euclidean distance 8 of the predicted flake RGB passed to the cluster-finding portion of the algorithm. The apparent bimodality is due to batch differences between the two wafer cassettes used in this experiment.

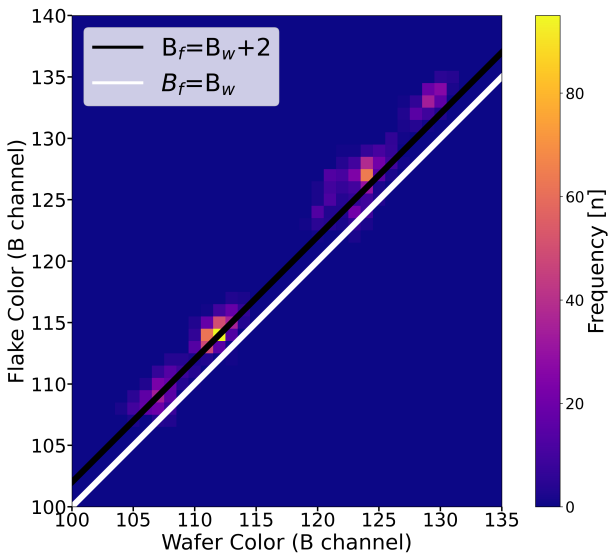


FIG. 23. Frequency of detected flake color vs local background color in the blue channel. The empirical function  $B_f=B_w+2$  was used to predict flake color from the background wafer color, with all pixels within Euclidean distance 8 of the predicted flake RGB passed to the cluster-finding portion of the algorithm. The apparent bimodality is due to batch differences between the two wafer cassettes used in this experiment.

- <sup>1</sup>H. Zhou, T. Xie, T. Taniguchi, K. Watanabe, and A. Young, “Superconductivity in rhombohedral trilayer graphene,” *Nature* **598**, 434–438 (2021).
- <sup>2</sup>H. Zhou, L. Holleis, Y. Saito, L. Cohen, W. Huynh, C. Patterson, F. Yang, T. Taniguchi, K. Watanabe, and A. Young, “Isospin magnetism and spin-polarized superconductivity in bernal bilayer graphene,” *Science* **375**, 774–778 (2022).
- <sup>3</sup>G. Chen, A. Sharpe, P. Gallagher, I. Rosen, E. Fox, L. Jiang, B. Lyu, H. Li, K. Watanabe, T. Taniguchi, J. Jung, Z. Shi, D. Goldhaber-Gordon, Y. Zhang, and F. Wang, “Signatures of tunable superconductivity in a tri-layer graphene moiré superlattice,” *Nature* **572**, 215–219 (2019).
- <sup>4</sup>G. Chen, A. Sharpe, E. Fox, S. Wang, B. Lyu, L. Jiang, H. Li, K. Watanabe, T. Taniguchi, M. Crommie, M. Kastner, Z. Shi, D. Goldhaber-Gordon, Y. Zhang, and F. Wang, “Tunable orbital ferromagnetism at noninteger filling of a moiré superlattice,” *Nano Letters* **22**, 238–245 (2022).
- <sup>5</sup>T. Han, Z. Lu, G. Souri, J. Sung, J. Wang, T. Han, K. Watanabe, T. Taniguchi, L. Fu, H. Park, and L. Ju, “Orbital multiferroicity in pentalayer rhombohedral graphene,” *Nature* **623**, 41–47 (2023).
- <sup>6</sup>Y. Cao, V. Fatemi, S. Fang, K. Watanabe, T. Taniguchi, E. Kaxiras, and P. Jarillo-Herrero, “Unconventional superconductivity in magic-angle graphene superlattices,” *Nature* **556** (2018).
- <sup>7</sup>A. Sharpe, E. Fox, A. Barnard, J. Finney, K. Watanabe, T. Taniguchi, M. Kastner, and D. Goldhaber-Gordon, “Emergent ferromagnetism near three-quarters filling in twisted bilayer graphene,” *Nature* **556** (2018).
- <sup>8</sup>Y. Xie, A. Pierce, J. Park, D. Parker, E. Khalaf, P. Ledwith, Y. Cao, S. Lee, S. Chen, P. Forrester, K. Watanabe, T. Taniguchi, A. Vishwanath, P. Jarillo-Herrero, and A. Yacoby, “Fractional chern insulators in magic-angle twisted bilayer graphene,” *Nature* **600**, 439–443 (2021).
- <sup>9</sup>T. Han, Z. Lu, G. Souri, J. Sung, J. Wang, T. Han, K. Watanabe, T. Taniguchi, H. Park, and L. Ju, “Correlated insulator and chern insulators in pentalayer rhombohedral-stacked graphene,” *Nature Nanotechnology* (2023).
- <sup>10</sup>K. Novoselov, A. Geim, S. Morozov, D. Jiang, Y. Zhang, S. Dubonos, I. Grigorieva, and A. Firsov, “Electric field effect in atomically thin carbon films,” *Science* **306**, 666–669 (2004).
- <sup>11</sup>A. Sidorov, M. Yazdanpanah, R. Jalilian, P. Ouseph, R. Cohn, and G. Sumanasekera, “Electrostatic deposition of graphene,” *Nanotechnology* **18** (2007).
- <sup>12</sup>F. Liu, “Mechanical exfoliation of large area 2d materials from vdw crystals,” *Progress in Surface Science* **96** (2021).
- <sup>13</sup>A. Ciesielski and P. Samori, “Graphene via sonication assisted liquid phase exfoliation,” *Chemical Society Review* **43** (2014).
- <sup>14</sup>J. H. Lee, E. K. Lee, W. J. Joo, Y. Jang, B. S. Kim, J. Y. Lim, S. H. Choi, S. J. Ahn, J. R. Ahn, M. H. Park, C. W. Yang, B. L. Choi, S. W. Hwang, and D. Whang, “Wafer-scale growth of single-crystal monolayer graphene on reusable hydrogen-terminated germanium,” *Science* **344**, 286–289 (2014).
- <sup>15</sup>C. Wang, W. Chen, C. Han, G. Wang, B. Tang, C. Tang, Y. Wang, W. Zou, W. Chen, X.-A. Zhang, S. Qin, S. Chang, and L. Wang, “Growth of millimeter-size single crystal graphene on cu foils by circumfluence chemical vapor deposition,” *Scientific Reports* **4** (2014).
- <sup>16</sup>D. Luo, D. Choe, R. Bizeo, M. Wang, H. Su, M. Huang, S. Jin, Y. Li, M. Kim, N. Pugno, B. Ren, Z. Lee, and R. Ruoff, “Folding and fracture of single-crystal graphene grown on a cu(111) foil,” *Advanced Materials* **34** (2022).
- <sup>17</sup>L. Banszerus, M. Schmitz, S. Engels, J. Dauber, M. Oellers, F. Haupt, K. Watanabe, T. Taniguchi, B. Beschoten, and C. Stampfer, “Ultrahigh-mobility graphene devices from chemical vapor deposition on reusable copper,” *Science Advances* **1** (2015).
- <sup>18</sup>Brookhaven National Laboratory, “Qpress,” Accessed November 17, 2023, <https://www.bnl.gov/qpress/>.
- <sup>19</sup>J. Xie, E. Regan, and F. Wang, Private Communication (2023).
- <sup>20</sup>X. Chen, F. Tian, C. Persson, W. Duan, and N.-x. Chen, “Interlayer interactions in graphites,” *Scientific Reports* **3** (2013).
- <sup>21</sup>E. Pop, V. Varshney, and A. Roy, “Thermal properties of graphene: fundamentals and applications,” *MRS Bulletin* **37** (2012).
- <sup>22</sup>R. Li, “Time-temperature superposition method for glass transition temperature of plastic materials,” *Materials Science and Engineering: A* **278**, 36–45 (2000).
- <sup>23</sup>S. Masubuchi, M. Morimoto, S. Morikawa, M. Onodera, Y. Asakawa, K. Watanabe, T. Taniguchi, and T. Machida, “Autonomous robotic searching and assembly of two-dimensional crystals to build van der waals superlattices,” *Nature Communications* **9** (2018).
- <sup>24</sup>E. Courtney and M. Pendharkar, “exfoliator step files,” Stanford Digital Repository, <https://purl.stanford.edu/zz730by7250> (2023).
- <sup>25</sup>N. Bittner, E. Courtney, M. Pendharkar, A. Sharpe, and D. Goldhaber-Gordon, “Algorithmic image recognition of few-layer van der waals’ materials,” (2024), in preparation (unpublished).
- <sup>26</sup>R. Nair, P. Blake, A. Grigorenko, K. Novoselov, T. Booth, T. Stauber, N. Peres, and A. Geim, “Fine structure constant defines visual transparency of graphene,” *Science* **320**, 1308 (2008).